Mars solar wind interaction: Formation of the Martian corona and atmospheric loss to space

Jean-Yves Chaufray, Ronan Modolo, François Leblanc, Gérard Chanteur, R. E. Johnson, J. G. Luhmann

Mars solar wind interaction: Formation of the Martian corona and atmospheric loss to space

J. Y. Chaufray,[1] R. Modolo,[2,3] F. Leblanc,[1,4] G. Chanteur,[5] R. E. Johnson,[6] and J. G. Luhmann[7]

[1]   A three-dimensional (3-D) atomic oxygen corona of Mars is computed for periods of low and high solar activities. The thermal atomic oxygen corona is derived from a collisionless Chamberlain approach, whereas the nonthermal atomic oxygen corona is derived from Monte Carlo simulations. The two main sources of hot exospheric oxygen atoms at Mars are the dissociative recombination of O_2^+ between 120 and 300 km and the sputtering of the Martian atmosphere by incident O^+ pickup ions. The reimpacting and escaping fluxes of pickup ions are derived from a 3-D hybrid model describing the interaction of the solar wind with our computed Martian oxygen exosphere. In this work it is shown that the role of the sputtering crucially depends on an accurate description of the Martian corona as well as of its interaction with the solar wind. The sputtering contribution to the total oxygen escape is smaller by one order of magnitude than the contribution due to the dissociative recombination. The neutral escape is dominant at both solar activities (1×10^{25} s^{-1} for low solar activity and 4×10^{25} s^{-1} for high solar activity), and the ion escape flux is estimated to be equal to 2×10^{23} s^{-1} at low solar activity and to 3.4×10^{24} s^{-1} at high solar activity. This work illustrates one more time the strong dependency of these loss rates on solar conditions. It underlines the difficulty of extrapolating the present measured loss rates to the past solar conditions without a better theoretical and observational knowledge of this dependency.

1.   Introduction

[2]   The history of the Martian oxygen escape is an important clue with regards to the evolution of the H_2O and CO_2 inventories of the Martian atmosphere. The history of the escape of the Martian atmosphere is usually divided into three epochs [*Tanaka*, 1986; *Hartmann and Neukum*, 2001; *Jakosky and Phillips*, 2001]. During the early Noachian 4.6 to 4.1 billion years ago, heavy meteoritic bombardment [*Melosh and Vickery*, 1989] and possibly a period of strong hydrodynamic escape [*Hunten*, 1973; *Hunten et al.*, 1987] could have removed large amounts of the atmosphere. During this period, large amounts of

phyllosilicates, observed by Omega on Mars Express, would have been formed by surface, near surface or deeper subsurface processes if Mars had an early dense atmosphere with a large aqueous reservoir [*Poulet et al.*, 2005; *Bibring et al.*, 2006]. At the end of the Noachian, between 4.1 Gyr and 3.8 Gyr ago, a global change of the climate occurred in association with significant volcanism (Tharsis formation), an intense late heavy meteoritic bombardment [*Gomes et al.*, 2005] and loss of the dynamo [*Acuña et al.*, 1998; *Stevenson*, 2001; *Chassefière et al.*, 2006]. Such a global change is also in agreement with recent chronology based on the alteration processes derived from mineralogy [*Bibring et al.*, 2006]. According to these authors, a large amount of water and sulphur (rapidly oxidized) could have been released by lavas during volcanic activity implying a transition from a nonacidic, aqueous phase alteration marked by production of phyllosilicates (''phyllosian'' era) to an acidic aqueous phase marked by production of sulfates (''theiikikan'' era). The evolution of the Martian atmosphere during the second main geological period (late Noachian, 4.1 to 3.8 Gyr ago and Hesperian between 3.7 and ~3 Gyr ago) may have been dominated by late outgassing [*Jakosky and Jones*, 1997] and significant atmospheric loss induced by the interaction of the solar wind with the upper atmosphere because of the lack of an intrinsic magnetic field [*Luhmann et al.*, 1992]. During

---

[1]Service d'Aéronomie du CNRS/Institut Pierre-Simon Laplace, Université Pierre et Marie Curie, Verrières-Le-Buisson, France.
[2]Swedish Institute of Space Physics, Uppsala, Sweden.
[3]Now at Department of Physics and Astronomy, University of Iowa, Iowa City, Iowa, USA.
[4]Temporarily at Osservatorio Astronomico di Trieste, Trieste, Italy.
[5]Centre d'Etude des Environnements Terrestres et Planétaires/Institut Pierre-Simon Laplace, Velizy, France.
[6]Department of Engineering Physics, University of Virginia, Charlottesville, Virginia, USA.
[7]Space Sciences Laboratory, University of California, Berkeley, Berkeley, California, USA.

the last period of the Martian history, the Amazonian (between ∼3 Gyr ago to present time), the dominant alteration process of the surface is an aqueous free alteration traced by the large amounts of anhydrous ferric oxides responsible of the red color of Mars [*Bibring et al.*, 2006]. The atmospheric evolution may have been characterized by sporadic outgassing phases [*Mangold et al.*, 2003], in relation with high obliquity phases [*Forget et al.*, 2006], and by significantly smaller atmospheric escape rates than during the early solar system history [*Leblanc and Johnson*, 2002]. Indeed, following all the theoretical work on the escape history of the Martian atmosphere (see reviews by *Chassefière and Leblanc* [2004] and *Chassefière et al.* [2006]), the fast decrease of the solar EUV flux intensity [*Lammer et al.*, 2003; *Ribas et al.*, 2005] appears to have played a major role.

[3] The current mechanisms for escape to space can be divided into two parts: thermal and nonthermal. The thermal escape or Jeans escape [*Chamberlain and Hunten*, 1987] is important for the light atmospheric constituents such as hydrogen and helium, whereas nonthermal escape processes dominate the escape of the heavier constituents such as oxygen, carbon and nitrogen [*Chassefière and Leblanc*, 2004].

[4] Six important nonthermal processes could be or could have been important in the history of the heavy species escape since the end of the Martian dynamo: (1) dissociative recombination of molecular ions, (2) acceleration of exospheric pickup ions by the solar wind, (3) charge exchange of these pickup ions leading to an O-ENA (energetic neutral oxygen atoms) escape, (4) sputtering of the atmosphere by reimpacting pickup ions, (5) ionospheric outflow and, in the case of nitrogen and carbon escape, and (6) molecular photodissociation [*Lammer et al.*, 2003; *Chassefière and Leblanc*, 2004; *Chassefière et al.*, 2006]. Dissociative recombination of O_2^+ with an electron in the Martian ionosphere between 120 and 200 km has been the first mechanism quoted as being potentially important [*McElroy*, 1972]. Such reactions in the upper atmosphere can produce hot oxygen atoms with energy from 0.4 eV up to 3.5 eV [*Kella et al.*, 1997], the escape energy of the oxygen atoms at these altitudes being around 2eV. These mechanisms are expected to have an important contribution to the current escape of the heavier components such as oxygen atoms, but also as carbon atoms by recombination of CO_2^+ [*Nagy et al.*, 2001; *Fox*, 2004; *Cipriani et al.*, 2007] and as nitrogen atoms by recombination of N_2^+ [*Brinkman*, 1971; *McElroy*, 1972; *Fox and Dalgarno*, 1983; *Fox*, 1993].

[5] These reactions have been extensively studied with 1-D models for present Martian conditions [*Ip*, 1988; *Nagy and Cravens*, 1988; *Kim et al.*, 1998; *Lammer et al.*, 2000; *Krestyanikova and Shematovitch*, 2005; *Cipriani et al.*, 2007], for past Martian conditions [*Zhang et al.*, 1993a] and with 3-D models for present Martian conditions [*Hodges*, 2000]. All these works conclude that the importance of this mechanism increases with the solar activity and that it is the main nonthermal mechanism leading to the formation of the current hot oxygen corona at solar minimum.

[6] The exospheric population can be ionized by EUV solar photons, solar wind electron impacts and charge exchange with the solar wind or planetary ions. Evidence for charge exchange between solar wind heavy ions and exospheric neutrals is the discovery of an X-ray halo within 3 Mars radii [*Dennerl et al.*, 2006] and detection of energetic neutral atoms (ENAs) by ASPERA 3 [*Barabash and Lundin*, 2006] on Mars Express [*Gunell et al.*, 2006; *Brinkfeldt et al.*, 2006]. Electronic impact ionization has been detected near the Magnetic Pileup Boundary by the Mars Global Surveyor observations [*Crider et al.*, 2000]. A fraction of these newly created ions can be picked up by the solar wind electric field and escape. The escape flux associated with this process has been estimated using a number of models: gas dynamic model [*Zhang et al.*, 1993b], 3-D Magneto-Hydrodynamic (MHD) models [*Ma et al.*, 2004; *Harnett and Winglee*, 2005] and 3-D Hybrid models [*Kallio and Janhunen*, 2002; *Modolo et al.*, 2005] (see also the review by *Nagy et al.* [2004] of the different mechanisms of interactions between the solar wind and the Martian atmosphere). This escape flux has been measured by the Phobos 2 mission [*Lundin et al.*, 1989; *Verigin et al.*, 1991] and more recently by ASPERA-3 on Mars Express [*Lundin et al.*, 2006; *Carlsson et al.*, 2006; *Kallio et al.*, 2006; *Barabash et al.*, 2007]. A fraction of the pickup ions can be neutralized in the exosphere leading to the formation of ENAs which can escape giving a third nonthermal escape mechanism.

[7] A fraction of the pickup ions and ENA can reimpact the atmosphere. These reimpacting populations can collide with the neutral atmospheric particles and producing recoils with enough energy to escape or to populate the Martian corona contributing a fourth nonthermal escape mechanism. This process, called atmospheric sputtering by pickup ions [*Johnson*, 1990], was applied to Mars for the first time by *Luhmann and Kozyra* [1991] using test particle approach, then using more realistic cross sections in an analytic model [*Luhmann et al.*, 1992]. Subsequently, 1-D or 3-D Monte Carlo simulations were carried out [*Kass and Yung*, 1995, 1996; *Johnson and Liu*, 1996; *Leblanc and Johnson*, 2001, 2002; *Cipriani et al.*, 2007]. This work showed that for the total production of nonthermal O escape, pickup ion sputtering is much smaller than loss due to dissociative recombination of O_2^+ at the present time for low solar conditions. However, it was thought that the sputtering process could have been the most important source of oxygen escape in the past [*Luhmann et al.*, 1992; *Luhmann*, 1997; *Leblanc and Johnson*, 2002] and could contribute in a significant way at present solar maximum conditions. Note that all these previous calculations were based on studies by *Luhmann et al.* [1992], who derived the reimpacting flux of accelerated O^+ picked up ions at different epochs of Mars' history using a gas dynamic approach.

[8] The fifth nonthermal escape process is the ionospheric outflow observed by ASPERA on Phobos 2 at high solar activity [*Lundin et al.*, 1989] and more recently by ASPERA 3 on Mars Express at low solar activity [*Lundin and Barabash*, 2004; *Dubinin et al.*, 2006; *Carlsson et al.*, 2006]. Such a mechanism is favored when the solar wind penetrates below the Martian ionopause [*Kar et al.*, 1996; *Fox*, 1997] as reported by *Lundin and Barabash* [2004]. This process has been studied recently by *Ma et al.* [2004] using a 3-D MHD model of the solar wind interaction with Mars. Ionospheric outflows may be responsible for the escape of ionospheric O_2^+ and CO_2^+ ions as observed by

ASPERA-3 but apparently in a less intense way than predicted [*Carlsson et al.*, 2006].

[9] A sixth mechanism, the photodissociation has been suggested as an important source for the nitrogen escape [*Brinkman*, 1971; *Fox and Dalgarno*, 1983; *Fox*, 1993] and carbon escape [*Fox and Bakalian*, 2001].

[10] In this paper, we describe the result of a consistent description of the interaction of the solar wind with Mars' upper atmosphere and corona. First we have calculated the thermal component of the oxygen and hydrogen corona by using Chamberlain exospheric theory [*Chamberlain*, 1963]. The nonthermal component of the oxygen corona is calculated as produced by dissociative recombination of the Martian O_2^+. Both components of the Martian corona are calculated at low and high solar activities. This corona was then used in a Mars 3-D hybrid model which determines the electromagnetic fields induced by the interaction of the solar wind with Mars' exosphere and atmosphere and calculates the 3-D ionization rates due to photoionization, solar wind electron impact and charge exchange in the Martian corona. In a third step, these ionization rates, electric and magnetic fields are introduced in a test particle simulation which is used to derive a 3-D picture of the Martian O^+ ion escape and reimpacting fluxes. Finally, the sputtering due to the reimpacting ions and ENAs below the exobase is calculated using 3-D Monte Carlo approach and the escape rates as well as the contribution to the Martian corona are estimated. This approach essentially mimics the approach used by *Luhmann et al.* [1992], the main difference with this previous work being the use of a 3-D hybrid model, particularly suited to describe the asymmetry of the Martian plasma environment, as well as a 3-D Martian corona taking into account thermal and nonthermal contributions.

[11] In section 2 we present the method used to describe the oxygen corona and the four nonthermal escape mechanisms which are dissociative recombination of O_2^+, pickup O^+ ions escape, O ENA escape and escape due to the sputtering from reimpacting O^+ pickup ions and O ENA. In section 3, each mechanism is described as it relates to the formation of the corona and escape. In section 4, discussion and comparisons of escape rates due to each mechanism are described.

2. Model

2.1. Oxygen and Hydrogen Coronas

2.1.1. Thermal Oxygen Corona

[12] Neutral coronas are computed on a spherical simulation grid. Grid points are distributed exponentially along the radial direction, with a spatial step varying from 4 km at 120 km height to 500 km at 3 R_m (Martian radii).

[13] Grid points are equally distributed in longitude and in the cosine of the co-latitude in order to have the same volume in each cell at a given altitude. Our simulation region is divided into two parts. Between 120 to 300 km, collisions are taken into account, whereas the region between 300 km and 3 R_m is assumed to be collisionless.

[14] For both solar minimum and solar maximum, the neutral atmosphere and the ionosphere used to describe the collisional domain are derived from *Krasnopolsky* [2002], who used an exospheric temperature equal to 200 K at low solar activity and equal to 350 K at high solar activity. The

description of the neutral atmosphere below 300 km in altitude is based on its two main heavy species: CO_2 which is the dominant species below roughly 200 km and O which is the dominant specie above 200 km. In order to simplify the description of the neutral atmosphere we describe the CO_2 as 3 atomic particles [*Johnson et al.*, 2000; *Leblanc and Johnson*, 2001]. Such an approximation has been shown to give a good estimate of the total escape rate of the oxygen atoms due to sputtering [*Leblanc and Johnson*, 2002]. The oxygen thermal component is obtained by using a 1-D model of Chamberlain's exosphere [*Chamberlain*, 1963] with exobase conditions derived from *Krasnopolsky* [2002]. In order to further speed up each run, we also neglect the rotation of the planet for the exospheric thermal component. According to *Kim and Son* [2000], the effect of the rotation becomes important only above 1000 km, depending on the longitude, but the thermal component is insignificant compared to the nonthermal component above 700 km (see further).

[15] Figure 1a shows the neutral atmosphere profiles used at low and high solar activities.

2.1.2. O_2^+ Dissociative Recombination Rates

[16] The hot, or nonthermal, oxygen corona is mainly produced by the dissociative recombination of O_2^+ ions. The ion profiles of *Krasnopolsky* [2002] have been obtained at a solar zenith angle equal to 60° (Figure 1a). We have assumed that these profiles are also a good first order approximation for SZA <60°. Actually, the temporal variability of the ionosphere may be large, particularly in the southern hemisphere due to the presence of the crustal magnetic field [*Krymskii et al.*, 2002; *Breus et al.*, 2004; *Withers and Mendillo*, 2005]. Due to rare in situ measurements of the Martian nightside ionosphere, we used a profile obtained by radio occultation during the Viking1 mission for SZA = 120° [*Zhang et al.*, 1990]. We also assumed that the production of hot O from O_2^+ is negligible at a solar zenith angle of 180°.

[17] The O_2^+ density profiles variation with the solar zenith angle is therefore given by

$$n\left(O_2^+\right) = n_{60} \qquad\qquad\qquad \text{for } 0° < \text{SZA} < 60°$$

$$n\left(O_2^+\right) = (n_{60} - n_{120})\cos(sza) + \frac{(n_{60} + n_{120})}{2} \quad \text{for } 60° < \text{SZA} < 120°$$

$$n\left(O_2^+\right) = 2n_{120}\cos(sza) + 2n_{120} \qquad \text{for } 120° < \text{SZA} < 180°$$

where n_{60} is the density profile at 60° and n_{120} at 120°.

[18] This model reproduces the O_2^+ profiles observed in situ by the Viking descent probes [*Hanson et al.*, 1977] below 250 km but overestimates it above 250 km. According to this model O_2^+ ions are dominant in the Martian ionosphere, therefore we neglect the other ionospheric species and we suppose that the electronic density is given by

$$n(e^-) = n\left(O_2^+\right) \qquad\qquad (1)$$

[19] This assumption is more questionable above 300 km where O^+ becomes important, but the production of hot
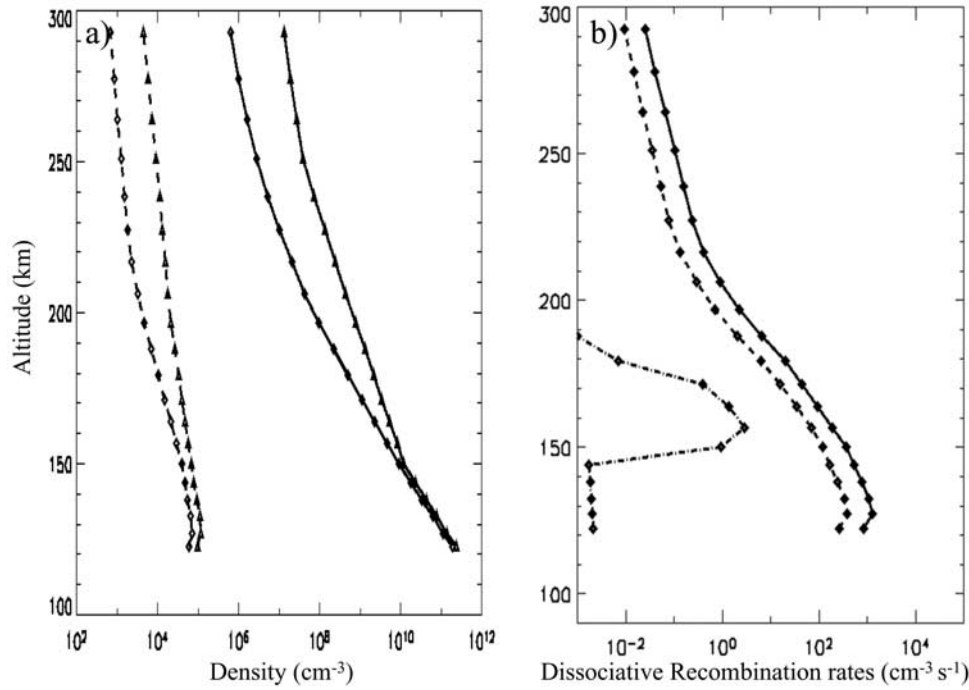
Figure 1. (a) Neutral atomic O (solid lines) and O_2^+ (dotted lines) density profiles in the Martian upper atmosphere used for solar maximum (triangles) and solar minimum conditions (squares) at SZA = 60° (derived from *Krasnopolsky* [2002]). (b) Photodissociation volumic production rate profiles for solar minimum at solar zenith angles equal to 0° (solid lines), 60° (dashed lines), and 120° (dot-dashed lines).

oxygen should not be important above 300 km because of the decrease of the O_2^+ density.

[20] The fast oxygen atom volumic production rate, $\alpha(z)$, is given by [*Peverall et al.*, 2001]

$$\alpha(z) = 2.4 \times 10^{-7} \left(\frac{300}{T_e}\right)^{0.70} n(e^-) n(O_2^+) \qquad (2)$$

[21] Figure 1b shows the volumic production rates for different solar zenith angles. The resulting total integrated hot oxygen production rate is 3×10^{27} O/s and 1×10^{28} O/s for the low and high solar activities. The production peaks correspond to the peaks in the O_2^+ density between 120 and 130 km.

2.1.3. Nonthermal Oxygen Corona

[22] The 3-D Monte Carlo approach used to calculate the exospheric spatial distribution has been described by *Leblanc and Johnson* [2001]. The algorithm to describe the collision between hot particles and the atmospheric cold background (Figure 1a) is derived from *Bird*'s [1994] approach. Such a collision is described using the universal potential of interaction [*Ziegler et al.*, 1985; *Johnson et al.*, 2000]. In order to limit the computing time, only the energetic particles are followed. We therefore introduced a cutoff energy defined as

$$E_{\min} = \frac{E_{escape}}{15} \qquad (3)$$

below which a hot particle is neglected.

[23] In Monte Carlo simulations, the weight of a test particle corresponds to the number of real particles described by a test particle. Figure 1b shows that the volume production rates can vary by more than 4 orders of magnitude. In order to describe such a dynamic range, we use a variable weight. The variation of the weight is given by

$$Weight(particle) = a \times P(cell) + b \qquad (4)$$

where $P(cell)$ is the production integrated on the volume of the cell where particles are initially produced, a and b are constants. In our model, the weight varies by 3 orders of magnitude from one thousandth to one tenth of the total integrated hot oxygen production P_{tot} given by

$$P_{tot} = \sum_{i=1}^{N_{cell}} P(i) \qquad (5)$$

[24] In this case a and b are given by

$$a = \frac{P_{tot}/10 - P_{tot}/1000}{P_{\max} - P_{\min}} \qquad (6)$$

$$b = P_{tot} \frac{P_{\max}/1000 - P_{\min}/10}{P_{\max} - P_{\min}} \qquad (7)$$

where $P_{\max}$ and $P_{\min}$ are the maximal and minimal value of $P(cell)$, respectively.

[25] At each step time Δt of 10 s, between approximately tens and approximately hundreds of pairs of fast O are produced by dissociative recombination (DR) and the energy of each fragment is divided equally between the two O atoms. The cell number k where the production occurred is obtained by solving the equation

$$\frac{\sum_{i=1}^{k-1} \frac{P(i)}{aP(i)+b}}{\sum_{i=1}^{N_{cell}} \frac{P(i)}{aP(i)+b}} < r < \frac{\sum_{i=1}^{k} \frac{P(i)}{aP(i)+b}}{\sum_{i=1}^{N_{cell}} \frac{P(i)}{aP(i)+b}} \quad . \tag{8}$$

where r is a random number between 0 and 1.

[26] For example, if we had assumed a constant weight W ($a = 0$ and $b = W$), this relation would be written as

$$\frac{\sum_{i=1}^{k} P(i)}{P_{tot}} < r < \frac{\sum_{i=1}^{k+1} P(i)}{P_{tot}} \tag{9}$$

in which case the production of hot O within the cells with a low production rate are badly described.

[27] In the other extreme, a weight equal to the production of the cell ($a = 1$, $b = 0$), the relation is written

$$\frac{k}{N_{cell}} < r < \frac{k+1}{N_{cell}} \tag{10}$$

[28] All the cells are equally described, but the only gain is a better description of the low production cells and it increases the number of test particles created in each time step and thereby the computation time of the simulation. We produce pairs of O atoms until the production simulated during Δt is greater than $P_{tot} \times \Delta t$. When this limit is reached the weight of the last couple is adjusted to force the total production simulated to be equal to the real production $P_{tot} \times \Delta t$.

[29] After producing the hot O, we follow each test particle with energy greater than E_{min} and calculate its trajectory. In each $dt = 0.05$ s ($\Delta t/200$), the number of collisions of a hot test particle with the cold atmosphere is computed and each collision is described using an impact parameter chosen randomly. The velocity of the cold test particle involved in the collision is derived from a Maxwellian distribution at the local temperature and its weight is equal to the weight of the hot test particle. The energetic recoiled particles produced collisionally are added to the population of test particles. We neglect the collisions between hot test particles.

[30] When a test particle crosses a cell, the density of the cell is updated by

$$n(cell) = n(cell) + weight(particle) * dt \tag{11}$$

and the velocity distribution function is similarly updated. At the end of the simulation, the density and the velocity distribution function are obtained by dividing the results by the total time of the simulation and by the volume of the cell.

[31] The use of an energy cutoff implies that below some altitude, the density computed is underestimated. We can determine the threshold altitude above which the density is not underestimated by

$$\frac{1}{R_t + R_m} = \frac{1}{R_x + R_m} - \frac{V_{min}^2}{2GM} \tag{12}$$

where R_t is the threshold altitude, R_x is the altitude between collision and collisionless regions (theoretically the exobase but to be conservative a limit that we chose at 300 km in our model), R_m the Martian radius, G is the gravitational constant, M the mass of Mars and V_{min} the velocity corresponding to the E_{min} kinetic energy. In the following results this value is $\sim$500 km. This limit should not influence significantly our results since the thermal oxygen component is dominant up to 550 km which is above the threshold altitude (see section 3).

[32] The simulation ends after having produced 2 million dissociations. In going from 600,000 dissociations to 2 million dissociations the average escape flux changes by less than 1%. We continue the simulation after 600,000 dissociations in order to reduce the statistical noise on the exospheric density.
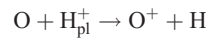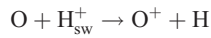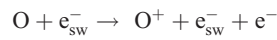
2.1.4. Hydrogen Corona

[33] The hydrogen corona is obtained by using a 1-D Chamberlain's exosphere with exobase conditions derived from *Krasnopolsky* [2002]. At low solar activity the hydrogen density at the exobase is 3.95×10^5 cm^{-3} and the temperature is equal to 200 K. At high solar activity the hydrogen density at the exobase is equal to 2.74×10^4 cm^{-3} and the temperature is equal to 350 K in agreement with exospheric temperatures derived from Lyman alpha emission by Mariner 6, 7 and 9 [*Anderson*, 1974; *Anderson and Hord*, 1971]. We do not include the hot hydrogen component which has been observed recently by Mars Express [*Chaufray et al.*, 2006; *Galli et al.*, 2006] because the origin of such a hot population is not clearly understood and its altitude and SZA dependencies not well constrained. The sensitivity of our results to the exobase temperature is discussed in the conclusion of this paper.

2.2. Exospheric Ions

[34] In order to model the escape and the precipitation of pickup ions produced by ionization of the Martian neutral corona, we coupled our oxygen and hydrogen coronas with a 3-D hybrid model [*Modolo et al.*, 2005] which describes the interaction of the solar wind plasma with the Martian neutral corona. In this model, electrons are described as a massless fluid, whereas ions are described as particles. The ions trajectories and the electric and magnetic fields are calculated by solving the motion and Maxwell equations using quasi-neutrality assumption. Hybrid models include in particular the description of the finite gyroradius, which is partly responsible for the asymmetry of the plasma in the vicinity of the planet. Hybrid approaches have been shown to be very relevant in situation where the gyroradius is of the same scale as the size of the interaction regions [*Brecht*, 1997; *Kallio et al.*, 1997; *Kallio and Koskinen*, 1999; *Shimazu*, 2001; *Kallio and Janhunen*, 2001, 2002; *Modolo et al.*, 2005]. In the model of *Modolo et al.* [2005], two solar ions H$^+$ and He^{++} and three planetary ions O$_2^+$, O$^+$ and H$^+$

are described. One of the original features of this model is the self-consistent description of the ionization of the Martian neutral corona by electron impact, charge exchange and photoionization. Production rates are here calculated at each time step from the calculated solar wind density and not fixed as an independent parameter. In such a way, mass loading is accurately and self-consistently described. The 3-D O and H density distributions are given in section 2.1. The photoionization frequency is roughly three times greater for oxygen and two times greater for hydrogen during maximum solar activity than during solar minimum activity [*Modolo et al.*, 2005].

[35]   The different processes of ionization of the Martian oxygen exosphere are

$$O + h\nu \rightarrow O^+ + e^-$$

$$O + e_{sw}^- \rightarrow O^+ + e_{sw}^- + e^-$$

$$O + H_{sw}^+ \rightarrow O^+ + H$$

$$O + H_{pl}^+ \rightarrow O^+ + H$$

where H_{pl}^+ is for planetary protons and H_{sw}^+ is for solar wind protons.

[36]   In the model, the O^+ ions created can be converted in ENA by charge exchange with the neutral exospheric component (H and O).

[37]   The 3-D hybrid model is calculated on a Cartesian grid whose x axis is the direction of the solar wind, the z axis is the magnetic field direction supposed to be aligned with the rotation axis in this study, and the y axis is defined in order to complete the reference frame. The region described is a box centered on Mars with a 19,200 km length along the x axis and a 45000 km length along the y and z axis with a constant spatial resolution equal to 300 km.

[38]   The ionization production rates and the electric and magnetic fields resulting from the hybrid simulation are then used as input parameters for a test particle Monte Carlo simulation which calculates the 3-D distribution of the precipitating flux. A few million of test particles are launched on the grid and the ion trajectories are numerically integrated using the standard charged particle equations of motion. In these simulations, a particle can be lost 3 ways. If it reaches the lower boundary at 300 km, the particle is recorded as an incident particle. If it reaches the upper boundary, it is recorded as an escape particle. If it is neutralized by charge exchange with neutral oxygen or hydrogen, it is recorded as an energetic neutral atom (ENA). Assuming momentum conservation during the charge exchange reaction, the ballistic trajectory of ENA is calculated from the velocity components of the parent ion. If this ENA crosses the lower boundary, it is recorded as an incident particle. If it crosses the upper boundary, it is considered an escaping neutral. Computation of the Martian neutral corona by a 3-D Monte Carlo model (step 1), their use in a 3-D multispecies hybrid model (step 2) and the calculation of the escaping and precipitating fluxes with a 3-D test particle simulation (step 3) are performed for both solar minimum and maximum conditions. These results are then used in the 3-D Monte Carlo model (step 4) in order to deduce the contribution of the sputtering process to the neutral oxygen corona.

2.3.   Atmospheric Sputtering

[39]   We consider only the reimpacting particles with an energy greater than E_{min}. We assume that all incident ions are neutralized by charge exchange reactions with atomic oxygen at 300 km without a significant loss of energy [*Luhmann and Kozyra*, 1991]. In order to evaluate the magnitude of the escape flux produced by incident low- and high-energy particles, we have made two simulations for both solar activity periods. In a first run we have computed the sputtering due to low-energy particles (between E_{min} and 500 eV) and in the second simulation we have calculated sputtering due to high-energy particles (greater than 500 eV). The model used to describe the sputtering of the Martian atmosphere is the same 3-D Monte Carlo model used for the description of the hot oxygen corona. The same atomic background atmosphere below 300 km (Figure 1a) and the same scheme to describe the collisions between hot particles and atmospheric thermalized particles below 300 km are used. The region above 300 km is assumed to be collisionless and therefore the hot component due to the dissociative recombination is not taken into account.

[40]   The surface at 300 km is divided into a resolution of 30×15 cells corresponding to a regular grid in longitude and a regular grid in cosines of the latitude. From the information of incident particles derived from the test particles model (step 3) energy and incident angle distributions of the precipitating flux are built for each cell.

[41]   The division between low- and high-energy particles allows us to show their relative importance for the escape flux, although the efficiency of the slow particles is lower than the efficiency of high-energy particles. It is interesting to highlight that the contribution of low-energy particles has also been suggested as a significant potential source of heating and sputtering of Titan's upper atmosphere [*Johnson et al.*, 2006]. For both solar activities we have launched several thousand incident particles: 100,000 at low energy and 15,000 at high energy.

[42]   The flux of precipitating particles which are not thermalized below 300 km (which cross the atmosphere) is added to the ENA escape computed previously (section 2.2).

3.   Variability of the Solar Wind
3.1.   Three-Dimensional Martian O Exosphere as Produced by Dissociative Recombination (Step 1)

[43]   Figure 2 displays the spatial distribution of the hot oxygen densities formed by the dissociative recombination for low solar activity (Figure 2a) and high solar activity (Figure 2b) in the equatorial plane.

[44]   As noted by *Hodges* [2000] in his Mars-L model, there is an important day to night contrast for both solar activities due to the low level of hot O production on the nightside. There is a small difference between sunset and sunrise profiles for the nonthermal component due to the
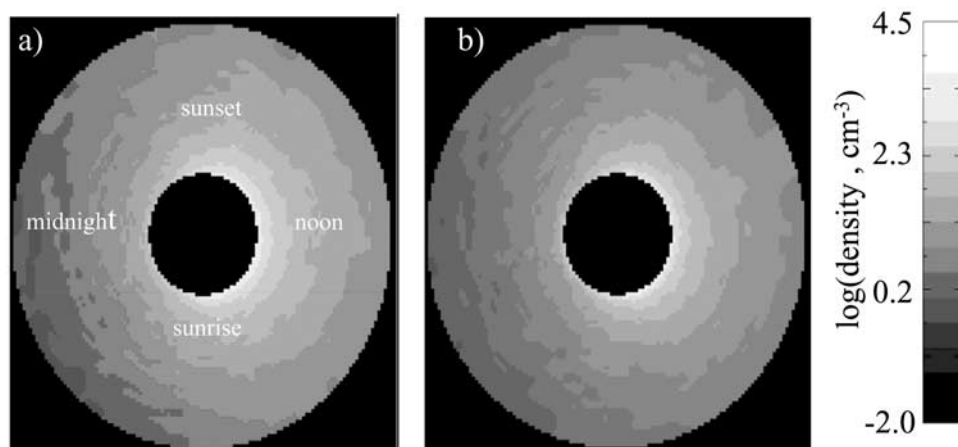
Figure 2. Hot oxygen density in the equatorial plane (a) for solar minimum conditions and (b) for solar maximum conditions due to dissociative recombination. The grey scale is a log scale of the O density in cm^{-3}. The dayside is on the right, and the nightside is on the left.

Martian rotation that we have considered in the case of the nonthermal component.

[45] Figure 3 displays the calculated oxygen density profiles at low and high solar activities (in the subsolar region) above 500 km. The contribution of the nonthermal oxygen corona due to dissociative recombination, has been added to the profiles of the thermal oxygen population. We have also displayed the hydrogen density profiles calculated in this work. The thin lines on the left represent the O density profiles resulting from the sputtering and will be discussed in section 3.4.

[46] The nonthermal part becomes dominant between 500 and 550 km at noon for low solar activity and between 750 and 800 km for high solar activity. For the Viking conditions (low solar activity), *Lammer et al.* [2000] have found equivalent altitude equal to 600 km, and for high solar activity model ("Nozomi model") to 500 and 550 km. For his "Nozomi model," *Lammer et al.* [2000] used a lower exospheric temperature. Indeed, these authors supposed that the exospheric temperatures deduced from Lyman alpha measurements [*Anderson*, 1974] could have been partially influenced by a hot component. A lower exosphere temperature could reduce the thermal part component and lower the altitude of the transition between the cold and the hot corona. The ratio between the oxygen densities at high and low solar activity is decreasing with altitude varying from 10 near 300 km to 2 at 6000 km. For low solar conditions, H is dominant above 300 km, whereas for high solar conditions it becomes dominant near 700 km.

[47] Our values for a low solar activity are roughly similar to the values obtained by *Hodges* [2000] in his Mars-L model and lower than those from *Kim et al.* [1998]. The difference is attributed to a different neutral density profile below 200 km in altitude. Indeed, while it seems evident that the O_2^+ ionospheric density profiles have a strong influence on the exospheric density profile of the hot atomic oxygen component, the neutral thermospheric density profile also is important as it thermalizes the hot population. For both solar activity conditions, the altitude range of production of the escaping oxygen is the region just below the exobase (170–190 km at solar min, and

200–230 at solar max). Below this altitude, most hot particles are thermalized and do not escape.

3.2. Pickup Ions and ENAs: Mass Loading

[48] Table 1 provides the total ionization rates by photoionization, solar wind electron impact and charge exchange with protons (column 1). Also included are their contribution to ion escape (column 2) and reimpacting rates (column 3). Because a fraction of the ions produced can
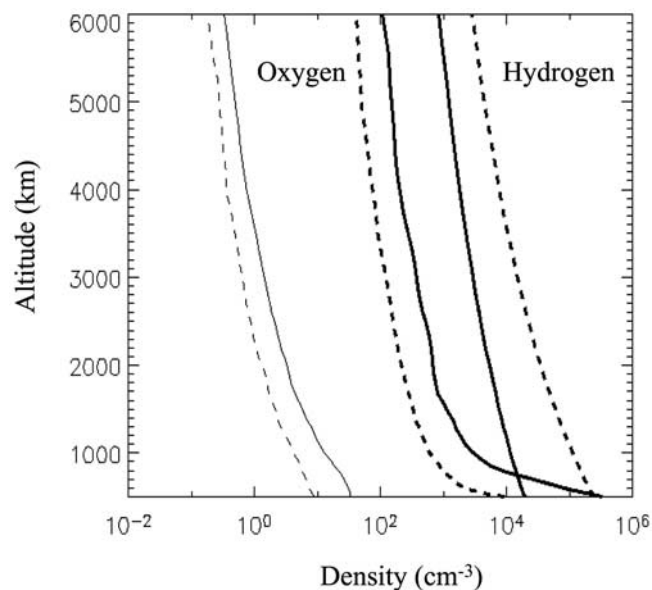
Figure 3. Oxygen and hydrogen densities above 300 km at high (solid line) and low (dotted line) solar activities. The oxygen profiles displayed are the sum of the cold population computed using Chamberlain's model and the hot population due to dissociative recombination at noon. The hydrogen density is assumed to be spherical and dominated by a cold population following Chamberlain's exospheric approach. The two thin lines on the left displaying the O density profiles resulting from the sputtering are given for information.

Table 1. Ion Production Rates and Ions Escaping and Precipitating Flux at the Exobase for Photoionization, Electronic Impacts, and Charge Exchange With Protons at Low and High Solar Activities[a]

	O^+ Total Production, s^{-1}	O^+ Escaping Flux, s^{-1}	O^+ Impacting Flux, s^{-1}	O Escaping Flux, s^{-1}	O Impacting Flux, s^{-1}
			Low Solar Activity		
Photoionization	1.6×10^{23}	3.2×10^{22}	1.2×10^{23}	2.0×10^{21}	1.1×10^{21}
Electronic impact	2.7×10^{22}	1.3×10^{22}	1.4×10^{22}	2.0×10^{20}	2.2×10^{20}
Charge exchange	1.7×10^{24}	1.6×10^{23}	1.5×10^{24}	6.8×10^{21}	1.0×10^{22}
			High Solar Activity		
Photoionization	6.7×10^{24}	2.8×10^{24}	3.4×10^{24}	2.7×10^{23}	2.4×10^{23}
Electronic impact	1.7×10^{23}	4.7×10^{22}	1.2×10^{23}	1.9×10^{21}	6.7×10^{21}
Charge exchange	2.5×10^{24}	6.1×10^{23}	1.7×10^{24}	7.1×10^{22}	1.2×10^{23}

[a]Shown are ion production rates (column 1) and ions escaping and precipitating flux at the exobase (columns 2 and 3) for photoionization (line 1), electronic impacts (line 2), and charge exchange with protons (line 3) at low and high solar activities. A part of the ionized particles created is neutralized by charge exchange with exospheric neutral hydrogen and oxygen atoms; this leads to the formation of energetic neutral atoms, which can escape to space (column 4) or reimpact the Martian atmosphere (column 5).

be converted into ENA by charge exchange with H and O coronas, we also give ENA escape (column 4) and reimpacting (column 5) rates derived from each mechanism.

[49] Our total ion production rates at low solar activity are equal to 1.6×10^{23}, 2.7×10^{22} and 1.7×10^{24} ions per second for photoionization, solar wind electron impact and proton charge exchange. They are significantly different than those obtained by *Zhang et al.* [1993b]. Their values were 6×10^{23}, 4.5×10^{24}, 4×10^{23} ions per second, respectively. These authors found that the main mechanism for O^+ ions production was electron impact, whereas in our model it is negligible for both solar conditions. These discrepancies are likely to be related to the electron impact production rates below the Magnetic Pileup Boundary (MPB) (at ~600 km above the subsolar region). In the hybrid 3-D model the solar wind electronic density and therefore the O^+ production rates by electronic impact decrease below this boundary, while for *Zhang et al.* [1993b], the obstacle is the ionopause at 300 km. This point is debated by *Krymskii and Breus* [1996] and *Luhmann* [1996]. In the hybrid code, the solar wind electron density reaches 10 cm^{-3} in the magnetic pileup region, the electron fluid is assumed to have an adiabatic motion with polytropic index equal to 2 with the ionization frequency proportional to the electron temperature [*Kim et al.*, 2004]. As a consequence, typical temperatures around 10^6 K are simulated. In the hybrid code the ionization frequency for electron impact varies with n_e^2 giving an ionization frequency in the magnetic pileup region equal to 2.1×10^{-7} s^{-1} that is four times lower than *Zhang et al.* [1993b]. The discrepancy in the photoionization production is less important due to a lower-density column of neutral oxygen in our exospheric model. The charge exchange between H^+ planetary ions and neutral oxygen which is not taken into account by *Zhang et al.* [1993b] partly explains the difference between our production rate by charge exchange and theirs. As an example, at solar minimum conditions, the total production rate due to charge exchange with solar wind protons is equal to 7.8×10^{23} s^{-1} ions (2 times larger than the value of *Zhang et al.* [1993b]), whereas the production rate due to planetary ions is equal to 9.1×10^{23} s^{-1}. For solar minimum the main mechanism of ionization is the charge exchange between exospheric neutral oxygen and planetary and solar wind protons. For solar maximum the main

mechanism of ionization is the photoionization in agreement with *Modolo et al.* [2005]. The contribution of charge exchange to the total O^+ ion production is larger at solar minimum than at solar maximum because of a larger hydrogen planetary density at solar minimum.

[50] A fraction of the O^+ ions produced in the exosphere by each mechanism is converted into energetic neutral atoms (ENAs) by charge exchange with the hydrogen and oxygen coronas.

[51] The proportion of O ENA produced (column 4 + column 5) with respect to the total O^+ production is low for both solar activities 1% and 8%, respectively. These production rates are lower than those calculated by *Barabash et al.* [2002], who find that 50% of ions produced are converted in ENA in the exosphere. But as they note, this result is very sensitive to the choice of the altitude of the lower boundary. Our lower boundary is set to 300 km, whereas *Barabash et al.* [2002] used a lower boundary at 210 km. The density scale height for a temperature equal to 200 K being ~30 km, the oxygen density varies from 210 km to 300 km by a factor ~20.

[52] The relative population of O^+ which reimpacts the atmosphere is greater for solar minimum conditions (84% of the total newly ionized O particles) than for solar maximum conditions (only 55%) (ratio between columns 3 + 5 and column 1). This difference can be explained by the deceleration of the solar wind due to the mass loading which happens further away from Mars at high solar activity than at low solar activity. The penetration of the solar wind is illustrated in Figure 4, which displays the magnitude of the electric field in the equatorial plane for low solar activity (Figure 4a) and high solar activity (Figure 4b). The region of penetration of the electric field is pushed out by ~300 km at high solar activity with respect to low solar activity. Such a decrease is not seen for electron impact ionization (lines 2 and 5 of Table 1) because electrons impacts occur essentially outside the region where the electric field is minimum, whereas photoionization and charge exchange with protons (planetary H^+) occurred in the region of minimum electric field. As a consequence, the energy and therefore the ion gyroradii are smaller near 300 km during maximum solar conditions than during minimum solar conditions. Typical trajectories of O^+ picked up ions are presented on Figure 4 to illustrate that point. Newly created picked up ions in the
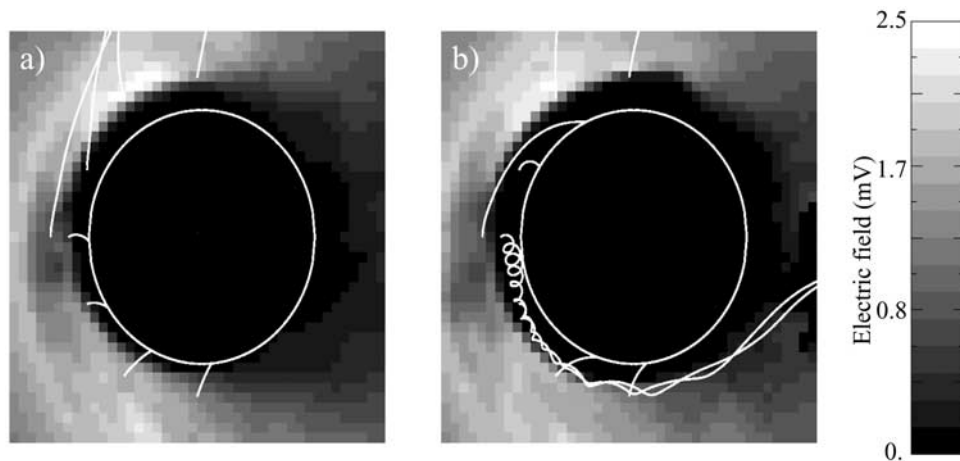
Figure 4. Magnitude of the solar wind electric field in the equatorial plane at (a) low solar activity and (b) high solar activity. Examples of trajectories of exospheric ions at different regions near the planet, in the equatorial plane, are also displayed. These exospheric ions can be produced by photoionization of the oxygen atoms, solar wind electron impacts with oxygen atoms, or charge exchange between solar wind (or planetary) protons with oxygen atoms. The white circle represents a sphere at 300 km in altitude. The pixel size is 300 km.

afternoon side of the minimum electric field region are more easily carried to the nightside because their gyroradii are too small to allow them to reimpact the planet. This agrees with the result of *Kallio and Janhunen* [2001], who have observed an anticorrelation between the proton precipitation in the Martian atmosphere and the O^+ production in their hybrid simulations, which they attribute to the shielding of the corona against the solar wind flow. To summarize, a dense exosphere increases the production of O^+ but also protects the planet by mass loading more efficiently the

incident solar wind. This has been considered by *Johnson and Luhmann* [1998] in the following way: an enhanced corona density can increase the minimum altitude above which ions that can reimpact the Martian atmosphere are produced and can therefore limit the reimpacting flux. The result presented in this paper is the first calculation confirming this suggestion. However, several improvements and tests need to be performed to fully describe this effect. First, these results have been obtained for standard solar wind conditions. A high-speed solar wind could penetrate
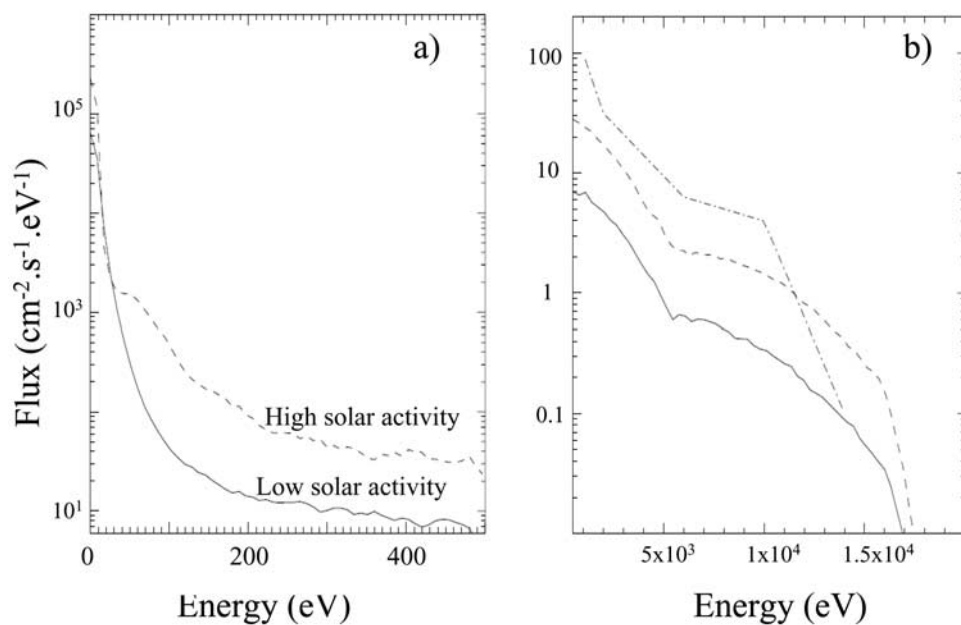

Figure 5. Energy distributions of the precipitating flux at low solar activity (solid line) and at high solar activity (dashed line). (a) Low-energy particles (energy between E_{min} and 500 eV). (b) High-energy particles (greater than 500 eV). The distributions obtained by *Luhmann et al.* [1992] are also given for comparison (1 EUV case) (dot-dashed line, Figure 5b).
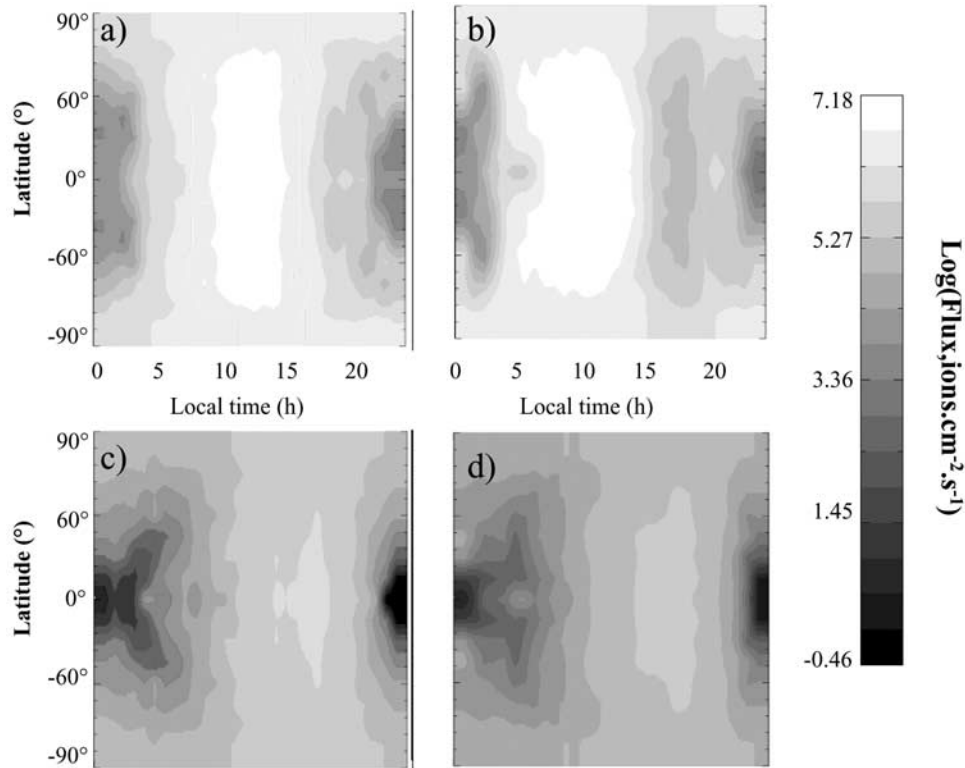
Figure 6. Spatial distributions of the precipitating flux at an altitude of 300 km above the Martian surface. The top row represents the distribution for the low-energy incident particles for (a) a period of low solar activity and (b) a period of high solar activity, and the bottom row displays the distribution for the high-energy incident particles for (c) a period of low solar activity and (d) a period of high solar activity. The symmetry about the equator has been imposed.

deeper in the atmosphere, as observed by ASPERA 3 [*Dubinin et al.*, 2006; *Lundin et al.*, 2006], and could therefore increase the precipitating flux. Moreover, it is critical refine the grid size of the hybrid model, particularly in between the Magnetic Pileup Boundary and the exobase. Indeed the spatial resolution of the hybrid model of *Modolo et al.* [2005] is equal to 300 km. Therefore the interpolation of the electric and magnetic fields in this region is a very rough approximation of the real structure and plasma intensity close to the Martian Magnetospheric Pileup Boundary.

3.3. Spatial Distribution of the Reimpacting Ions

[53] The energy distributions of the precipitating flux of O^+ and O ENA are displayed in Figure 5 for both solar activities and for the low- and high-energy particles. We have also displayed the distributions obtained by *Luhmann et al.* [1992] for their 1EUV model and energies above one keV (dot-dashed line). The shapes of the distributions are similar for the three models (Figure 5b). There is a factor of 4 between the high-energy precipitating flux at high solar conditions and the high-energy precipitating flux at low solar conditions.

[54] Figure 6 shows the spatial distributions of the precipitating flux for both solar conditions and for low- and high-energy particles. The electric field of convection is oriented along Mars' east-west axis. In this paper, we neglected Mars' obliquity so that the only asymmetry

induced by the electric field of convection is along the east-west axis. This is why we impose a symmetry about the equator in the reimpacting flux. In the case of high-energy particles (Figures 6c and 6d), particles precipitate into the Martian atmosphere is on the evening side rather than on the morning side because of the direction of the electric field is from evening to morning sides. The particles impacting the Martian atmosphere with high energies are produced at high altitudes. Ions produced on the morning side are simply accelerated away from Mars. In the case of low-energy particles, particles with energy between 0 and 30 eV dominate the precipitating flux, as seen in Figure 6, and most of them impact the planet on the dayside around the subsolar region. As shown on Figure 4, at high solar activity, a fraction of the ions created near the subsolar region can reimpact the planet near sunrise.

[55] The acceleration region is clearly moved further away from the planet's exobase by the mass loading which has a strong effect on the pickup ion population. However, the magnitude of the difference between solar minimum and maximum activities depends on several parameters that have not been completely described here. One of them is a grid size better adapted to the height scale of the ionosphere and exosphere. A better grid size could change our result, but should not change the effect of the mass loading on the reimpacting flux. Other parameters, like the solar wind speed, the solar wind short time variability and

Table 2. Incident and Escape Fluxes for the Sputtering in s^{-1} at Low and High Solar Activities for Low-Energy Particles and High-Energy Particles[a]

	Low-Energy Particles	High-Energy Particles
Low Solar Conditions		
Incident flux	1.6×10^{24}	3.6×10^{22}
Escape flux	9.8×10^{22}	1.1×10^{23}
High Solar Conditions		
Incident flux	5.3×10^{24}	1.4×10^{23}
Escape flux	2.9×10^{23}	4.2×10^{23}

[a]Shown are incident and escape fluxes for the sputtering in s^{-1} at low and high solar activities for low-energy particles (column 1) and high-energy particles (column 2). The value of 500 eV has been arbitrary chosen as the limit between low- and high-energy particles.

the interplanetary magnetic field orientation could also influence this result.

3.4. Corona Density and Escape Induced by Sputtering

[56] The sputter contribution by the low- and high-energy particles reimpacting the Martian exosphere, given in Table 2, are seen to be similar in size.

[57] The efficiency of sputtering is given by the ratio between the escape flux and the precipitating particle flux. The efficiency is greater for high-energy particles (around 3) than for low-energy particles (around 0.06). The peak in the production of escaping O is near 170 km at low solar conditions and near 200 km at high solar conditions. This is slightly below the exobase and below the peak for escape produced by dissociative recombination.

[58] The equatorial distribution of the exospheric oxygen density due to sputtering is displayed in Figure 7a for low solar activity and in Figure 7b for high solar activity. The density distribution resulting is essentially related to the spatial distribution of the precipitating particles. The highest densities are observed where the reimpacting fluxes are also the highest. It is clear when comparing Figures 7 and 2 that the sputter contribution to the exosphere is significantly

lower than the contribution due to the dissociative recombination at both solar activities. This comparison shows a posteriori that our description of the solar wind interaction with Mars, in which we consider only the dissociative recombination contribution to the Martian corona, will not be changed significantly by taking into account sputtering.

[59] The velocity distribution functions in the exosphere are displayed in Figure 8 at three different local times: noon (Figure 8a), sunset (Figure 8b) and sunrise (Figure 8c) equatorial regions at high solar activity for dissociative recombination (top row) with a constant velocity resolution equal to ~300 m s^{-1} and for sputtering (bottom row) with a velocity resolution varying from ~900 m s^{-1} for velocities lower than 10 km s^{-1} to ~125 km s^{-1} for velocities higher than 110 km s^{-1}. The sign of the tangential velocity is positive when one particle moves from noon to sunset. The radius of the white circle is equal to the escape velocity. All ballistic trajectories have velocities in this circle. In agreement with exosphere theory, escape velocities exist only in the positive radial velocity hemisphere. Satellites trajectories have velocities in the inner region delimited by the pair of hyperbolae. In those regions, in the case of dissociative recombination (top row) we do not have such a population in agreement with exospheric theory [*Chamberlain and Hunten*, 1987]. Because the resolution used to describe the velocity distribution function is three times lower, this depletion is not visible in the case of the sputtering. In the case of dissociative recombination, our results are similar to those obtained by *Hodges* [2000] in his Mars L model. At noon (Figure 8a), the velocity function distributions are symmetric with respect to the radial velocity axis. At sunset (Figure 8b), a larger proportion of those particles with a negative radial velocity has a positive tangential velocity, whereas at sunrise (Figure 8c) a larger proportion of those particles with a negative radial velocity has a negative tangential velocity. This is due to the fact that most of the particles are produced near noon. Velocities are limited to 6000−7000 m/s which correspond to an energy equal to 3.5 eV for a particle at 300 km. In the case of sputtering, an extended wing of the oxygen velocity function distributions
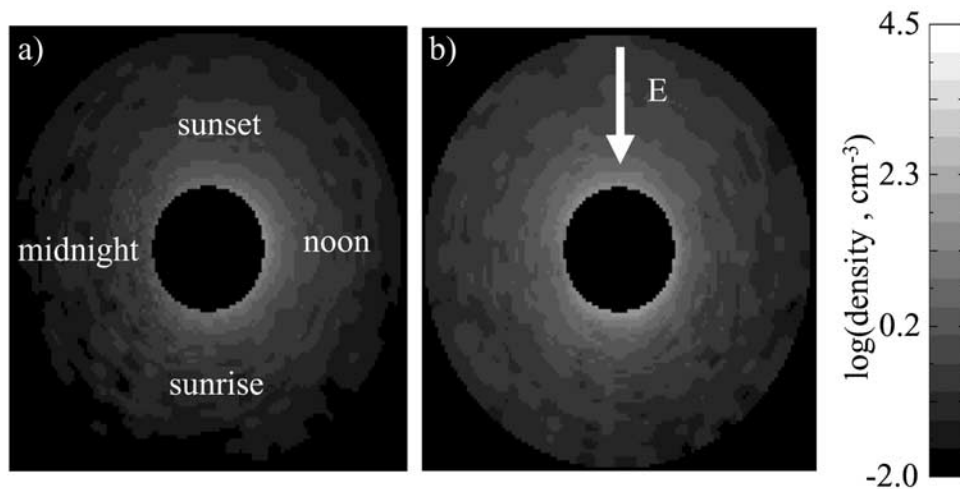

Figure 7. Hot oxygen density due to the sputtering for (a) minimum and (b) maximum solar conditions in the equatorial plane (the grey scale is in log10 of cm^{-3}). The dayside is on the right, and the nightside is on the left. Contributions of the sputtering due to low- and high-energy particles have been added.
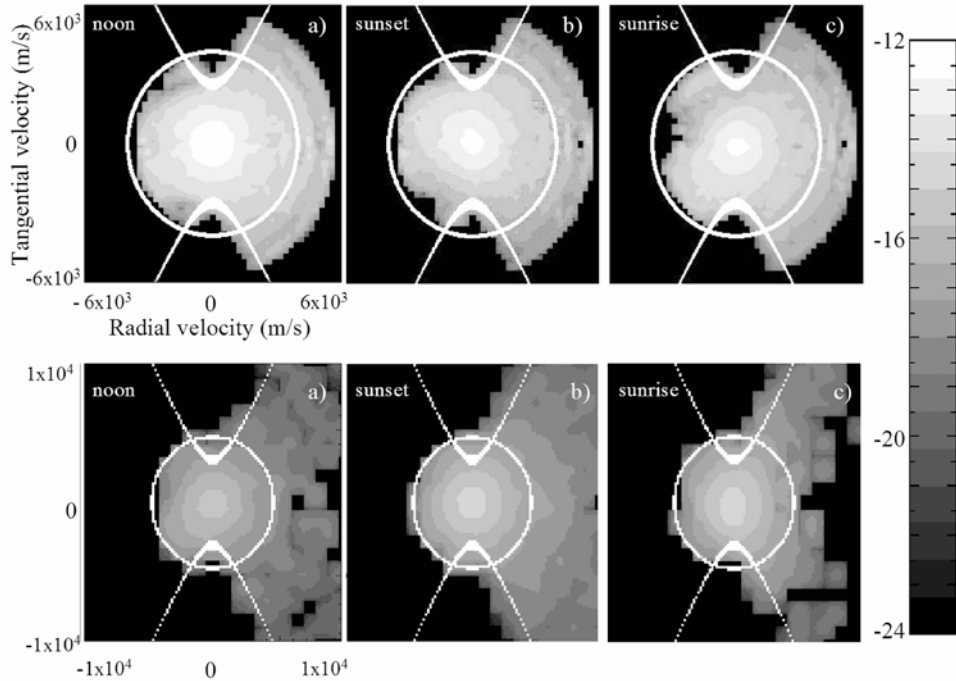
Figure 8. Velocity distribution functions between 560 and 890 km. The top row shows dissociative recombination and the bottom row shows sputtering at noon, sunset, and sunrise for solar maximum conditions (in log10 of $cm^{-6} \cdot s^3$). The white circles give the local escape speed, and the white hyperbolae give the velocities of atoms with periapses at ~720 km.

is observed in agreement with *Cipriani et al.* [2007], particularly at sunset where high-energy particles are reimpacting preferentially (Figure 6d).

4. Escape Rates at Low and High Solar Activity

[60] At both extremes of solar activity, the main mechanism responsible for oxygen escape is the dissociative recombination (Table 3). At low solar activity (Table 3, column 1), the value calculated in this paper is 3 to 4 times lower than the value of the "L-model" of *Hodges* [2002] equal to 4.4×10^{25} s^{-1} and lower than the value obtained by *Kim et al.* [1998] equal to 3.4×10^{25} s^{-1} after a correction [*Nagy et al.*, 2001]. More recently, *Krestyanikova and Shematovitch* [2005] and *Cipriani et al.* [2007] have estimated the oxygen escape flux using the 1-D solar minimum profiles of *Krasnopolsky* [2002] in the thermosphere and found a flux equal to 6.5×10^{24} s^{-1} and 5.5×10^{24} s^{-1}, which are slightly smaller than our present calculated rates.

[61] At high solar activity (Table 3, column 2), the escape flux due to dissociative recombination in our model is equal to 4×10^{25} s^{-1}. It is smaller than *Hodges* [2002] (1.8×10^{26} s^{-1}), *Kim et al.* [1998] (8.5×10^{25} s^{-1}) and *Krestyanikova and Shematovitch* [2005] (1.1×10^{26} s^{-1}), but the ratio between low and high solar activities, equal to 0.25, is in agreement with *Cipriani et al.* [2007] and *Hodges* [2002]. The difference with the model of *Krestyanikova and Shematovitch* [2005] is probably due to our simplification in the treatment of the collisions. Because we assume an atomic background atmosphere, all the collisions are described by a single interaction potential. *Cipriani et al.* [2007] show that

the universal potential for O-O collisions in the energy range of DR products over estimates the thermalization rate compared to a more accurate differential cross section [*Kharchenko et al.*, 2000] and therefore reduces the escape rate. Our total ion escape flux (line 2) at low solar activity is equal to 2×10^{23} s^{-1}, which is slightly smaller than previous estimates by *Barabash et al.* [2002], *Ma et al.* [2004], and *Modolo et al.* [2005] (who include ionospheric bulk escape), because our calculation of the O exospheric density leads to a globally less dense exosphere than used in those works and do not describe the ionospheric bulk escape.

[62] At high solar activity, our ion escape flux is equal to 3.4×10^{24} s^{-1}, a value slightly larger than *Modolo et al.* [2005], who find 2.4×10^{24} s^{-1}. They found a ratio between escape flux at high and low solar activities of 5, whereas in this paper we found a ratio equal to 17. This large difference is due to the thermal oxygen component which is assumed to be almost the same for both solar activities by *Modolo et al.* [2005], whereas in our model the

Table 3. Escape Flux Calculated at Low and High Solar Activities in s^{-1} [a]

	Low Solar Activity	High Solar Activity
Dissociative recombination	1×10^{25}	4×10^{25}
Ion escape	2×10^{23}	3×10^{24}
ENA escape	4×10^{22}	4×10^{23}
Sputtering	2×10^{23}	7×10^{23}

[a]ENA escape due to charge exchange of O^+ ions in the exosphere corresponds to the neutral escape given in Table 1, column 4, and the precipitating particles neutralized below 300 km.

thermal component is denser at high solar activity than at low solar activity. The crustal field pushed out the magnetic boundaries [*Ma et al.*, 2004] and therefore should decrease the escape flux. *Ma and Nagy* [2007] show that the O^+ escape flux is reduced by 25% when they consider crustal field at subsolar point compared to the case where the crustal field is at anti-solar point.

[63] *Verigin et al.* [1991] give a heavy ion escape flux equal to 5×10^{24} s^{-1} using measurement by the TAUS instrument on Phobos 2. This is in good agreement with our result, whereas *Lundin et al.* [1989] using measurements by ASPERA on Phobos 2 estimated the ion escape flux equal to 2.5×10^{25} s^{-1}. This is higher than our estimate by nearly one order of magnitude. Recently, *Barabash et al.* [2007] used measurements by Aspera 3 on board Mars Express for low solar activity to obtain 1.6×10^{23} s^{-1} in very good agreement with our estimate. This observation seems to confirm the strong influence of the solar activity on the ion escape. Since Aspera 3 cannot measure ions with energy below 30 eV, their estimate is a lower bound to the ion escape flux.

[64] The escape flux of oxygen ENAs due to charge exchange of O^+ with exospheric hydrogen and oxygen is also given (line 3). It is slightly different from Table 1, column 4, because the precipitating flux given in Table 1, column, 5 has been calculated at 300 km from the surface rather than the exobase. Solar activity is also seen to have a strong influence on the ENA escape.

[65] Escape fluxes due to the sputtering (line 4) are insignificant at low and high solar activities. This result differs from previous publications [*Leblanc and Johnson*, 2001] because we have used a self consistent approach to calculate the flux of picked up ion reimpacting the Martian atmosphere. However, this result also illustrates that the reimpacting flux could have been significantly larger in the past because of a stronger EUV flux and a faster solar wind. This can lead to a more intense electric field in the past and therefore to a larger and more energetic flux of reimpacting particles than at present [*Luhmann et al.*, 1992; *Leblanc and Johnson*, 2001]. The velocity of the solar wind has two consequences for the sputtering rate. The first one is to increase the solar wind dynamic pressure and therefore the depth of penetration of the solar wind into the Martian atmosphere [*Dubinin et al.*, 2006]. The second one is on the energy of the precipitating pickup ions, since the maximum energy of a pickup ion is proportional to the square of the solar wind velocity.

5. Conclusion

[66] In this paper, we have described consistently four nonthermal mechanisms producing oxygen escape, dissociative recombination of O_2^+, pickup ion escape, ENA escape and sputtering induced loss, at both low and high solar activity. We show that dissociative recombination is the main mechanism leading to oxygen escape and to hot oxygen corona formation in the present epoch at both low and high solar activity. The difference with earlier work is primarily due to the mass loading of the solar wind which reduces the reimpacting ion flux and hence the sputtering, a process suggested by *Johnson and Luhmann* [1998] as possibly affecting the escape in earlier epochs.

[67] This study illustrates the importance of properly and self consistently coupling an accurate model of the Martian exosphere with a 3-D model of the Martian magnetosphere able to describe finite gyroradius effects. However, it also is clear that an accurate coupling of a 3-D thermosphere and ionosphere model can affect these results. Seasonal variabilities of the thermosphere in both latitude and longitude should have significant consequences for the interaction of the solar wind with the Martian atmosphere. The crustal magnetic field may also induce significant local effects but has been shown to be negligible when the global interaction of the solar wind with Mars is considered [*Ma et al.*, 2004].

[68] The main limitation of this work is the spatial resolution of the hybrid 3-D model (300 km). This affects our description of the variation in the solar wind–Mars interaction from low to high solar activities. Another limitation is the ionospheric sources not taken into account in this study which contribute to the solar wind mass loading [*Carlsson et al.*, 2006]. Using a more realistic 3-D O_2^+ profiles, which reproduces better the observations [e.g., *Ma et al.*, 2004] would be an improvement of our model.

[69] The thermal hydrogen and oxygen density profiles play an important role in the interaction of the solar wind with the Martian atmosphere. Thermal oxygen is the main source of production of O^+ ions, whereas protons created by the ionization of the Martian hydrogen corona are a key source of O^+ production by charge exchange. Chamberlain's approach used in this work to describe the density of the hydrogen corona or the cold component of the oxygen corona implies a strong dependence on the exobase temperature which is still poorly known at Mars. Measurement of hydrogen exospheric temperatures up to 350 K at high solar activity by Mariner 6, 7 and 9 missions [*Anderson*, 1974] have been recently discussed by *Lichtenegger et al.* [2006], who suggested that it could have been artificially enhanced by the presence of a hot hydrogen component. Such temperatures are in disagreement with recent estimates of the exobase temperature around 200 K obtained during Mars Global Surveyor and Mars Odyssey aerobraking between 170 and 180 km [*Keating et al.*, 1998, 2003; *Bougher et al.*, 2000; *Tracadas et al.*, 2001] and are inconsistent with solar cycle variations of peak plasma densities [*Lichtenegger et al.*, 2004]. Recent observations by ASPERA-3 [*Barabash and Lundin*, 2006] and SPICAM [*Bertaux et al.*, 2006; *Leblanc et al.*, 2006] could help to better understand this inconsistency, such as the recent observations of the Lyman alpha emission in the Martian exosphere which suggest the presence of a hot Martian hydrogen component [*Galli et al.*, 2006; *Chaufray et al.*, 2006]. A smaller variation of the exospheric temperature from low to high solar activities would imply a lower mass loading during high solar activity could result in a larger flux of energetic particles reimpacting the Martian atmosphere and therefore a larger escape flux at high solar activity. This emphasizes the main conclusion of this work: new progress in understanding of Mars-Solar wind interaction will be possible only by self consistently coupling a 3-D magnetospheric model with smaller spatial resolution to a thermospheric model with a temperature that is accurately determined for a given solar activity.

[70] Such an effort would be required to accurately describe the atmospheric loss rates in the present epoch,

before attempting to extrapolate to solar conditions in earlier epochs, during which the solar UV/EUV flux was most probably significantly larger and the solar wind was faster and denser than today. A very recent analysis by *Ma and Nagy* [2007] shows the importance of the solar wind dynamic pressure in the global escape. Simple extrapolations of the present observed erosion rates to the whole history of Mars should clearly provide large underestimate of the total cumulate atmospheric loss.

References

Acuña, M. H., et al. (1998), Magnetic field and plasma observations at Mars: Initial results of the Mars Global Surveyor MAG/ER experiment, *Science*, *279*, 1676–1680.

Anderson, D. E. (1974), Mariner 6, 7 and 9 Ultraviolet Spectrometer Experiment: Analysis of hydrogen Lyman alpha data, *J. Geophys. Res.*, *79*, 1513–1518.

Anderson, D. E., and C. W. Hord (1971), Mariner 6 and 7 Ultraviolet Spectrometer Experiment: Analysis of hydrogen Lyman-alpha data, *J. Geophys. Res.*, *76*, 6666–6673.

Barabash, S., and R. Lundin (2006), ASPERA-3 on Mars Express, *Icarus*, *182*, 301–307.

Barabash, S., M. Holmström, A. Lukyanov, and E. Kallio (2002), Energetic neutral atoms at Mars: 4. Imaging of planetary oxygen, *J. Geophys. Res.*, *107*(A10), 1280, doi:10.1029/2001JA000326.

Barabash, S., A. Fedorov, R. R. Lundin, and J.-A. Sauvaud (2007), Martian atmospheric erosion rates, *Science*, *315*, 501–503, doi:10.1126/science.1134358.

Bertaux, J.-L., et al. (2006), SPICAM on Mars Express: Observing modes and overview of UV spectrometer data and scientific results, *J. Geophys. Res.*, *111*, E10S90, doi:10.1029/2006JE002690.

Bibring, J. P., et al. (2006), Global mineralogical and aqueous Mars history derived from OMEGA/Mars Express data, *Science*, *312*, 400–404.

Bird, G. A. (1994), *Molecular Gas Dynamics and the Direct Simulation of Gas Flows*, Clarendon, Oxford, U. K.

Bougher, S. W., S. Engel, R. G. Roble, and B. Foster (2000), Comparative terrestrial planet thermospheres: 3. Solar cycle variation of global structure and winds at solstices, *J. Geophys. Res.*, *105*, 17,669–17,692.

Brecht, S. H. (1997), Solar wind protons deposition in the Martian atmosphere, *J. Geophys. Res.*, *102*, 11,287–11,294.

Breus, T. K., A. M. Krymskii, D. H. Crider, N. F. Ness, D. Hinson, and K. K. Barashyan (2004), Effect of the solar radiation in the topside atmosphere/ionosphere of Mars: Mars Global Surveyor observations, *J. Geophys. Res.*, *109*, A09310, doi:10.1029/2004JA010431.

Brinkfeldt, K., et al. (2006), First ENA observations at Mars: Solar-wind ENAs on the nightside, *Icarus*, *182*, 439–447, doi:10.1016/j.icarus.2005.12.023.

Brinkman, R. T. (1971), Mars: Has nitrogen escaped?, *Science*, *179*, 944–945.

Carlsson, E., et al. (2006), Mass composition of the escape plasma at Mars, *Icarus*, *182*, 320–328.

Chamberlain, J. W. (1963), Planetary coronae and atmospheric evaporation, *Planet. Space Sci.*, *11*, 901–960.

Chamberlain, J. W., and D. M. Hunten (1987), Book-Review—Theory of Planetary Atmospheres, *Science*, *238*, 96.

Chassefière, E., and F. Leblanc (2004), Mars Atmospheric escape and evolution: interaction with the solar wind, *Planet. Space Sci.*, *52*, 1039–1058.

Chassefière, E., F. Leblanc, and B. Langlais (2006), The combined effects of escape and magnetic field histories at Mars, *Planet. Space Sci.*, *55*, 343–357, doi:10.1016/j.pss.2006.02.003.

Chaufray, J. Y., E. Quémerais, J.-L. Bertaux, and F. Leblanc (2006) Sounding of the Martian upper atmosphere with SPICAM on Mars Express, abstract 00566 presented at First Europlanet Scientific Conference, Berlin, 18–22 Sept.

Cipriani, F., F. Leblanc, and J. J. Berthelier (2007), Martian corona: Nonthermal sources of hot heavy species, *J. Geophys. Res.*, *112*, E07001, doi:10.1029/2006JE002818.

Crider, D., et al. (2000), Evidence of the electron impact ionization in the magnetic pile-up boundary of Mars, *Geophys. Res. Lett.*, *27*, 45–48.

Dennerl, K., C. M. Lisse, A. Bhardwaj, V. Burwitz, J. Englhauser, H. Gunnel, M. Holmström, F. Jansen, and V. Kharchenko (2006), First observation of Mars with XMM-Newton: High resolution X-ray spectroscopy with RGS, *Astron. Astrophys.*, *451*, 709–722, doi:10.1051/0004-6361:20054253.

Dubinin, E., et al. (2006), Electric fields within the Martian magnetosphere and ion extraction: ASPERA 3 observations, *Icarus*, *182*, 337–342.

Forget, F., R. M. Haberle, F. Montmessin, B. Levrard, and J. W. Head (2006), Formation of glaciers on Mars by atmospheric precipitation at high obliquity, *Science*, *311*, 368–371, doi:10.1126/science.1120335.

Fox, J. L. (1993), The production and escape of nitrogen atoms on Mars, *J. Geophys. Res*, *98*, 3297–3310.

Fox, J. L. (1997), Upper limits to the outflow of ions at Mars, *Geophys. Res. Lett.*, *24*, 2901–2904.

Fox, J. L. (2003), Effect of H_2 on the Martian ionosphere: Implications for atmospheric evolution, *J. Geophys. Res.*, *108*(A6), 1223, doi:10.1029/2001JA000203.

Fox, J. L. (2004), CO_2^+ dissociative recombination: A source of thermal and nonthermal C on Mars, *J. Geophys. Res.*, *109*, A08306, doi:10.1029/2004JA010514.

Fox, J. L., and F. M. Bakalian (2001), Photochemical escape of atomic carbon from Mars, *J. Geophys. Res.*, *106*, 28,785–28,795.

Fox, J. L., and A. Dalgarno (1983), Nitrogen escape from Mars, *J. Geophys. Res.*, *88*, 9027–9032.

Galli, A., P. Wurz, H. Lammer, M. H. I. Lichtenegger, R. Lundin, S. Barabash, A. Grigoriev, M. Holmström, and H. Gunell (2006), The hydrogen exospheric density profiles measured with ASPERA-3/NPD, *Space Sci. Rev.*, *126*, 447–467, doi:10.1007/s11214-006-9089-7.

Gomes, R., H. Levison, K. Tsiganis, and A. Morbidelli (2005), Origin of the cataclysmic late heavy bombardment of the terrestrial planets, *Nature*, *435*, 466–469, doi:10.1038/nature03676.

Gunell, H., et al. (2006), First ENA observations at Mars: Charge exchange ENAs produced in the magnetosheath, *Icarus*, *182*, 431–438, doi:10.1016/j.icarus.2005.10.027.

Hanson, W. B., S. Sanatani, and D. R. Zuccaro (1977), The Martian ionosphere as observed by the Viking retarding potential analyzers, *J. Geophys. Res.*, *82*, 4351–4363.

Harnett, E. M., and R. M. Winglee (2005), Three-dimensional fluid simulations of plasma asymmetries in the Martian magnetotail caused by the magnetic anomalies, *J. Geophys. Res.*, *110*, A07226, doi:10.1029/2003JA010315.

Hartmann, W. K., and G. Neukum (2001), Cratering chronology and the evolution of Mars, *Space. Sci. Rev.*, *96*, 165–194.

Hodges, R. R. (2000), Distributions of hot oxygen for Venus and Mars, *J. Geophys. Res*, *105*, 6971–6981.

Hodges, R. R., Jr. (2002), The rate of loss of water from Mars, *Geophys. Res. Lett.*, *29*(3), 1038, doi:10.1029/2001GL013853.

Hunten, D. M. (1973), The escape of light gases from planetary atmospheres, *J. Atmos. Sci.*, *30*, 1481–1494.

Hunten, D. M., R. O. Pepin, and J. C. G. Walker (1987), Mass fractionation in hydrodynamic escape, *Icarus*, *69*, 532–549.

Ip, W.-H. (1988), On a hot oxygen corona of Mars, *Icarus*, *76*, 134–145.

Jakosky, B. M., and J. H. Jones (1997), The history of Martian volatiles, *Rev. Geophys.*, *35*, 1–16.

Jakosky, B. M., and R. J. Phillips (2001), Mars volatile and climate history, *Nature*, *412*, 237–244.

Johnson, R. E. (1990), *Energetic Charged-Particle Interaction With Atmospheres and Surfaces*, Springer, New York.

Johnson, R. E., and M. Liu (1996), The loss of the atmosphere from Mars, *Science*, *274*, 1932–1933.

Johnson, R. E., and J. G. Luhmann (1998), Sputter contribution to the atmospheric corona on Mars, *J. Geophys. Res*, *103*, 3649–3653.

Johnson, R. E., D. Schnellenberger, and M. C. Wong (2000), The sputtering of an oxygen thermosphere by energetic O^+, *J. Geophys. Res.*, *105*(E1), 1659–1670.

Johnson, R. E., M. Michael, O. J. Tucker, V. I. Shematovich, J. G. Luhmann, and S. A. Ledvina (2006), Plasma-ion-induced sputtering and heating of Titan's atmosphere, paper presented at the First Europlanet Scientific Conference, Berlin, 18–22 Sept.

Kallio, E., and P. Janhunen (2001), Atmospheric effects of proton precipitation in the Martian atmosphere and its connection to the Mars-solar wind interaction, *J. Geophys. Res.*, *106*(A4), 5617–5634.

Kallio, E., and P. Janhunen (2002), Ion escape from Mars in a quasi-neutral hybrid model, *J. Geophys. Res.*, *107*(A3), 1035, doi:10.1029/2001JA000090.

Kallio, E., and H. Koskinen (1999), A test particle simulation of the motion of oxygen ions and solar wind protons near Mars, *J. Geophys. Res*, *104*, 557–579.

Kallio, E., J. G. Luhmann, and S. Barabash (1997), Charge exchange near Mars: The solar wind absorption and energetic neutral production, *J. Geophys. Res*, *102*, 22,183–22,197.

Kallio, E., et al. (2006), Ion escape at Mars: Comparison of a 3-D hybrid simulation with Mars Express IMA/ASPERA-3 measurements, *Icarus*, *182*, 350–359, doi:10.1016/j.icarus.2005.09.018.

Kar, J., K. K. Mahajan, and R. Kohli (1996), On the outflow of O_2^+ ions at Mars, *J. Geophys. Res.*, *101*, 12,747–12,752.

Kass, D. M., and Y. L. Yung (1995), The loss of atmosphere from Mars due to solar wind-induced sputtering, *Science*, *268*, 697–699.

Kass, D. M., and Y. L. Yung (1996), The loss of atmosphere from Mars: Response, *Science*, *274*, 1932–1933.

Keating, G. M., et al. (1998), The structure of the upper atmosphere of Mars: In situ accelerometer measurements from Mars Global Surveyor, *Science*, *279*, 1672–1676.

Keating, G. M., M. Theriot, R. Tolson, S. Bougher, F. Forget, and J. Forbes (2003), Global measurements of the Mars upper atmosphere: In situ accelerometer measurements from Mars Odyssey 2001 and Mars Global Surveyor, *Proc. Lunar Planet. Sci. Conf. 36th*, *36th*, Abstract 1142.

Kella, J., P. J. Johnson, H. B. Pederson, L. Vejby-Christensen, and L. H. Andersen (1997), The source of green light emission determined from a heavy-ion storage ring experiment, *Science*, *276*, 1530–1533.

Kharchenko, V., A. Dalgarno, B. Zygelman, and J.-H. Yee (2000), Energy transfer in collisions of oxygen atoms in the terrestrial atmosphere, *J. Geophys. Res.*, *105*, 24,899–24,906.

Kim, J., A. F. Nagy, J. L. Fox, and T. E. Cravens (1998), Solar cycle variability of hot oxygen atoms at Mars, *J. Geophys. Res*, *103*, 29,339–29,342.

Kim, Y. H., and S. Son (2000), The effects of planetary rotation on the exospheric density distributions of the Earth and Mars, *J. Korean Astron. Soc.*, *33*, 127–135.

Kim, Y. K., et al. (2004), Electron-impact ionization cross section database (version 3.0), Natl. Inst. of Stand. and Technol., Gaithersburg, Md., 23 Aug. (Available at http://physics.nist.gov/ionxsec)

Krasnopolsky, V. A. (2002), Mars' upper atmosphere and ionosphere at low, medium, and high solar activities: Implications for evolution of water, *J. Geophys. Res.*, *107*(E12), 5128, doi:10.1029/2001JE001809.

Krestyanikova, M. A., and V. I. Shematovich (2005), Stochastic models of hot planetary and satellite coronas: A photochemical source of hot oxygen in the upper atmosphere of Mars, *Sol. Syst. Res.*, *39*, 22–32.

Krymskii, A. M., and T. K. Breus (1996), Comment on "Oxygen ions rates at Mars and Venus: Relative contributions of impact ionization and charge exchange" by M. H. Zhang, J. G. Luhmann, A. F. Nagy, J. R. Spreiter, and S. S. Stahara, *J. Geophys. Res.*, *101*(E3), 7599–7602.

Krymskii, A. M., T. K. Breus, N. F. Ness, M. H. Acuña, J. E. P. Connerney, D. H. Crider, D. L. Mitchell, and S. J. Bauer (2002), Structure of the magnetic field fluxes connected with crustal magnetization and topside ionosphere at Mars, *J. Geophys. Res.*, *107*(A9), 1245, doi:10.1029/2001JA000239.

Lammer, H., W. Stumptner, and S. J. Bauer (2000), Upper limits for the Martian exospheric number density during the Planet B/Nozomi mission, *Planet. Space Sci.*, *48*, 1473–1478.

Lammer, H., H. I. M. Lichtenegger, C. Kolb, I. Ribas, E. F. Guinan, R. Abart, and S. J. Sauer (2003), Loss of water from Mars: Implications for the oxidation of the soil, *Icarus*, *165*, 9–25.

Leblanc, F., and R. E. Johnson (2001), Sputtering of the Martian atmosphere by solar wind pick-up ions, *Planet. Space Sci.*, *49*, 645–656.

Leblanc, F., and R. E. Johnson (2002), Role of molecular species in pickup ion sputtering of the Martian atmosphere, *J. Geophys. Res.*, *107*(E2), 5010, doi:10.1029/2000JE001473.

Leblanc, F., J. Y. Chaufray, J. Lilensten, O. Witasse, and J.-L. Bertaux (2006), Martian dayglow as seen by the SPICAM UV spectrograph on Mars Express, *J. Geophys. Res.*, *111*, E09S11, doi:10.1029/2005JE002664.

Lichtenegger, H. I. M., H. Lammer, D. F. Vogl, and S. J. Bauer (2004), Temperature effects of energetic neutral hydrogen on the Martian exosphere, *Adv. Space Res.*, *33*, 140–144.

Lichtenegger, H. I. M., H. Lammer, Y. N. Kulikov, S. Kazeminejad, G. H. Molina-Cuberos, R. Rodrigo, B. Kazeminejad, and G. Kirchengast (2006), Effects of low energetic neutrals atoms to Martian and Venusian exospheric temperature estimations, *Space Sci. Rev.*, *126*, 469–501, doi:10.1007/s11214-006-9082-1.

Luhmann, J. G. (1996), Reply, *J. Geophys. Res.*, *101*(E3), 7603–7605.

Luhmann, J. G. (1997), Correction to "The ancient oxygen exosphere of Mars: Implications for atmospheric evolution," *J. Geophys. Res*, *102*, 1637.

Luhmann, J. G., and J. U. Kozyra (1991), Dayside pickup oxygen precipitation at Venus and Mars: Spatial distributions, energy deposition and consequences, *J. Geophys. Res*, *96*, 5457–5468.

Luhmann, J. G., R. E. Johnson, and M. H. G. Zhang (1992), Evolutionary impact of sputtering of the Martian atmosphere by O⁺ pick-up ions, *Geophys. Res. Lett.*, *19*, 2151–2154.

Lundin, R., and S. Barabash (2004), Evolution of the Martian atmosphere and hydrosphere: Solar wind erosion studied by ASPERA-3 on Mars Express, *Planet. Space Sci.*, *52*, 1059–1071.

Lundin, R., A. Zakharov, R. Pellinen, H. Borg, B. Hultqvist, N. Pissarenko, E. M. Dubinin, S. Barabash, I. Liede, and H. Koskinen (1989), First measurement of the ionospheric plasma escape from Mars, *Nature*, *341*, 609–612.

Lundin, R., et al. (2006), Ionospheric plasma acceleration at Mars: ASPERA-3 results, *Icarus*, *182*, 308–319.

Ma, Y.-J., and A. F. Nagy (2007), Ion escape fluxes from Mars, *Geophys. Res. Lett.*, *34*, L08201, doi:10.1029/2006GL029208.

Ma, Y., A. F. Nagy, I. V. Sokolov, and K. C. Hansen (2004), Three-dimensional, multispecies, high spatial resolution MHD studies of the solar wind interaction with Mars, *J. Geophys. Res.*, *109*, A07211, doi:10.1029/2003JA010367.

Mangold, N., F. Costard, and F. Forget (2003), Debris flows over sand dunes on Mars: Evidence for liquid water, *J. Geophys. Res.*, *108*(E4), 5027, doi:10.1029/2002JE001958.

McElroy, M. B. (1972), Mars: An evolving atmosphere, *Science*, *175*, 443–445.

Melosh, H. J., and I. M. Vickery (1989), Impact erosion of the primordial atmosphere of Mars, *Nature*, *338*, 487–489.

Modolo, R., G. M. Chanteur, E. Dubinin, and A. P. Matthews (2005), Influence of the solar activity on the Martian plasma environment, *Ann. Geophys*, *23*, 433–444.

Nagy, A. F., and T. E. Cravens (1988), Hot oxygen atoms in the upper atmospheres of Venus and Mars, *Geophys. Res. Lett.*, *15*, 433–435.

Nagy, A. F., M. W. Liemohn, J. L. Fox, and J. Kim (2001), Hot carbon densities in the exosphere of Mars, *J. Geophys. Res*, *82*, 4341–4349.

Nagy, A. F., et al. (2004), The plasma environment of Mars, *Space Sci. Rev.*, *111*, 33–114, doi:10.1023/B:SPAC.0000032718.47512.92.

Peverall, R., S. Rosen, R. R. Peterson, M. Larsonn, A. Al-Khalili, L. Viktor, J. Semaniak, R. Bobbenkamp, A. N. Le Padellec, and W. J. Van der Zande (2001), Dissociative recombination and excitation of O₂⁺: Cross sections, products yields, and implications for studies of ionospheric airglows, *J. Chem. Phys.*, *114*, 6679–6689.

Poulet, F., J.-P. Bibring, J. F. Mustard, A. Gendrin, N. Mangold, Y. Langevin, R. E. Arvidson, B. Gondet, and C. Gomez (2005), Phyllosilicates on Mars and implications for early Martian climate, *Nature*, *438*, 623–627, doi:10.1038/nature04274.

Ribas, I., E. F. Guinan, M. Güdel, and M. Audard (2005), Evolution of the solar activity over time and effects on planetary atmospheres. I. High-energy irradiances (1–1700 Å), *Astrophys. J.*, *622*, 680–694, doi:10.1086/427977.

Shimazu, H. (2001), Three-dimensional hybrid simulation of solar wind interaction with unmagnetized planets, *J. Geophys. Res.*, *106*, 8333–8342.

Stevenson, D. J. (2001), Mars' core and magnetism, *Nature*, *412*, 214–219.

Tanaka, K. L. (1986), The stratigraphy of Mars, Proc. Lunar Planet. Sci. Conf. 17th, Part 1, *J. Geophys. Res.*, *91*, suppl., E139–E158.

Tracadas, P. W., M. T. Zuber, D. E. Smith, and F. G. Lemoine (2001), Density structure of the upper thermosphere of Mars from measurements of air drag on the Mars Global Surveyor spacecraft, *J. Geophys. Res*, *106*, 23,349–23,358.

Verigin, M. I., et al. (1991), Ions of planetary origin in the Martian magnetosphere (Phobos 2/TAUS experiment), *Planet. Space Sci.*, *39*, 131–137.

Withers, P., and M. Mendillo (2005), Response of peak electron densities in the Martian ionosphere to day-to-day changes in solar flux due to solar rotation, *Planet. Space Sci.*, *53*, 1401–1418, doi:10.1016/j.pss.2005.07.010.

Zhang, M. H. G., J. G. Luhmann, and A. J. Kliore (1990), An observational study of the nightside ionospheres of Mars and Venus with radio occultation methods, *J. Geophys. Res*, *95*, 17,095–17,102.

Zhang, M. H. G., J. G. Luhmann, S. W. Bougher, and A. F. Nagy (1993a), The ancient oxygen exosphere of Mars: Implication for atmospheric evaluations, *J. Geophys. Res*, *98*, 10,915–10,923.

Zhang, M. H. G., J. G. Luhmann, A. F. Nagy, J. R. Spreiter, and S. Stahara (1993b), Oxygen ionization rates at Mars and Venus: Relative contributions of impact ionization and charge exchange, *J. Geophys. Res*, *98*, 3311–3318.

Ziegler, J. F., J. P. Biersack, and V. Littmark (1985), *The Stopping and Ranges of Ions in Solids*, Pergamon, New York.

––––––––––––––––

G. Chanteur, Centre d'Etude des Environnements Terrestres et Planétaires, I.U.T. de Vélizy, 10–12, Avenue de l'Europe, F-78140 Velizy, France.

J. Y. Chaufray, Service d'Aéronomie du CNRS, Réduit de Verrières - BP 3, Route des Gatines, F-91371 Verrières le Buisson Cédex, France. (chaufray@aerov.jussieu.fr)

R. E. Johnson, Department of Engineering Physics, School of Engineering and Applied Science, University of Virginia, 116 Engineer's Way, P.O. Box 400745, Charlottesville, VA 22904-4745, USA.

F. Leblanc, Osservatorio Astronomico di Trieste, Via Tiepolo 11, I-34143 Trieste, Italy.

J. G. Luhmann, Space Sciences Laboratory, University of California, Berkeley, 7 Gauss Way, Berkeley, CA 94720-7450, USA.

R. Modolo, Department of Physics and Astronomy, University of Iowa, 203 Van Allen Hall, Iowa City, IA 52242-1479, USA.